JFM RAPIDS
journals.cambridge.org/rapids

Turbulence structure behind the shock in canonical shock–vortical turbulence interaction

Jaiyoung Ryu[1],[‡] **and Daniel Livescu**[1],[†]

[1]CCS-2, Los Alamos National Laboratory, Los Alamos, NM 87545, USA

The interaction between vortical isotropic turbulence (IT) and a normal shock wave is studied using direct numerical simulation (DNS) and linear interaction analysis (LIA). In previous studies, agreement between the simulation results and the LIA predictions has been limited and, thus, the significance of LIA has been underestimated. In this paper, we present high-resolution simulations which accurately solve all flow scales (including the shock-wave structure) and extensively cover the parameter space (the shock Mach number, M_s, ranges from 1.1 to 2.2 and the Taylor Reynolds number, Re_λ, ranges from 10 to 45). The results show, for the first time, that the turbulence quantities from DNS converge to the LIA solutions as the turbulent Mach number, M_t, becomes small, even at low upstream Reynolds numbers. The classical LIA formulae are extended to compute the complete post-shock flow fields using an IT database. The solutions, consistent with the DNS results, show that the shock wave significantly changes the topology of the turbulent structures, with a symmetrization of the third invariant of the velocity gradient tensor and (M_s-mediated) of the probability density function (PDF) of the longitudinal velocity derivatives, and an M_s-dependent increase in the correlation between strain and rotation.

Key words: compressible turbulence, shock waves, turbulence simulation

1. Introduction

Turbulent flows interacting with shock waves occur in many areas, including internal and external hypersonic flight, combustion, inertial confinement fusion and astrophysics. Due to the very large range of spatio-temporal scales of the problem and complicating effects such as rapid changes in the thermodynamic state across the shock, a detailed understanding of this interaction remains far from reach. In general,

the shock width is much smaller than the turbulence scales, even at low shock Mach number, M_s, and it becomes comparable to the molecular mean free path at high M_s values. At larger M_s values, the flow equations themselves depart from the classical Navier–Stokes equations and fully resolved simulations of both the shock and the turbulence with extended hydrodynamics at practically relevant Reynolds numbers will not be feasible for the foreseeable future.

When viscous and nonlinear effects can be neglected across the shock, the interaction with turbulence can be treated analytically for small-amplitude disturbances by assuming the shock as a perturbed discontinuity and using the linearized Euler equations and Rankine–Hugoniot jump conditions. In order to derive analytical solutions, a single plane wave moving at an angle ψ with respect to the shock is considered first. Then the solutions for the flow and thermodynamic variables behind the shock are obtained as a superposition of plane wave solutions, assuming that each plane wave component of turbulence independently interacts with the shock. This approach is called linear interaction analysis (LIA) (Moore 1954; Ribner 1954). Since LIA was introduced in the 1950s, a number of studies have presented comparisons between LIA and numerical simulations. Due to the high cost to resolve all the turbulence scales, as well as the shock width, previous studies using direct numerical simulation (DNS) (Lee, Lele & Moin 1993; Jamme *et al.* 2002) could consider weak shocks only ($M_s \leqslant 1.5$) in regimes where the interaction was dominated by viscous and/or nonlinear effects and, consequently, showed limited agreement with the LIA solutions. More recently, using shock-capturing schemes, the range of M_s values was extended considerably (Lee, Lele & Moin 1997; Mahesh, Lele & Moin 1997; Larsson & Lele 2009; Larsson, Bermejo-Moreno & Lele 2013). As an attempt to approach the infinite Reynolds number limit using the simulation database, Larsson *et al.* (2013) artificially removed viscous dissipation behind the shock wave using Reynolds stress budget terms. A good agreement was achieved for the streamwise variation of the turbulent kinetic energy, but individual Reynolds stresses and their ratios did not match the LIA solutions.

Experimental realizations of this problem are also very challenging, due to problems in controlling the shock wave and difficulties in taking measurements close to the shock wave. Barre, Alem & Bonnet (1996) have studied the interaction at $M_s = 3$ and showed a good agreement for the amplification of streamwise velocity fluctuations with LIA. Agui, Briassulis & Andreopoulos (2005) also found a good agreement for the same quantity at $M_s = 1.04$; however, at higher M_s their results are considerably higher than the LIA solution. Thus, as a result of the limited agreement presented in previous studies, the significance of LIA has not yet been fully appreciated. This also led to the recent proposal of a universal amplification parameter (Donzis 2012) which contradicts the M_s-dependent LIA predictions.

There have been a number of studies on the variation of the Reynolds stresses and their transport equations, vorticity fluctuations, length scales, anisotropic states of post-shock turbulence, and energy spectra behind the shock wave using numerical and experimental data (Andreopoulos, Agui & Briassulis 2000; Larsson *et al.* 2013). However, to the authors' knowledge, the local structure of post-shock turbulence has not yet been investigated in detail. Therefore, here, we reassess the importance of LIA for the shock–turbulence interaction (STI) problem and attempt to fill some important gaps in our knowledge of turbulence undergoing this interaction.

In this study, using fully resolved simulations extensively covering the parameter space, we show that the DNS results do converge to the LIA solutions as M_t becomes small (even when the Taylor Reynolds number, Re_λ, is not very large) and emphasize

the importance of the theory in many practical applications when the shock width is much smaller than the turbulence scales. In order to examine higher-order turbulence statistics, we extend the classical LIA formulae to compute the full post-shock flow fields using an isotropic turbulence (IT) database. The LIA solutions are used to examine the turbulence structures immediately behind the shock wave for high-M_s interaction problems, where fully resolved DNS are not feasible.

2. Numerical details

We have conducted fully resolved simulations of STI in an open-ended domain with lateral periodic boundary conditions and the reference frame moving with a shock wave. The compressible Navier–Stokes equations with the perfect gas assumption are solved using the compressible version of the CFDNS code (Livescu *et al.* 2009; Petersen & Livescu 2010). The ratio of specific heats is $\gamma = 1.4$, the viscosity varies with the temperature as $\mu = \mu_0(T/T_0)^{0.75}$, and the Prandtl number is $Pr = 0.7$. The flow variables are non-dimensionalized by the upstream mean density, temperature and speed of sound. The spatial discretization is performed using sixth-order compact finite differences (Lele 1992) and the variable time step Runge–Kutta–Fehlberg (RK45) method is used for time advancement. An accelerating layer $\sim 10\%$ of the domain length is used at the outflow boundary (Freund 1997) to ensure non-reflecting boundary conditions. The sensitivity of the results to the outflow boundary conditions has been tested by repeating the simulation with 2π, 4π and 6π domain lengths in the streamwise direction using simple sine waves and also for the full STI problem. The results presented here for the 4π domain show no noticeable wave reflections at the boundary or influence of the accelerating layer on the domain of interest around the shock. The mean shock drifts slightly in time (as also observed by Larsson & Lele 2009), with the speed increasing with M_s for the accelerating layer used here. The largest drift speed, obtained for $M_s = 2.2$, was approximately 0.1% of the free-stream velocity, and significantly smaller at lower values of M_s. The results presented in this paper remain the same whether the statistics are computed at fixed locations or moving with the drifting shock.

The number of mesh points is large enough such that all flow scales, including the shock width (δ) and the Kolmogorov length scale (η) upstream and downstream of the shock wave, are accurately resolved without applying any shock-capturing or filtering methods. At least 12 grid points are used in the streamwise direction across the shock wave. Shock-front corrugation is also well resolved in the transverse directions, which is important to accurately predict the evolution of transverse velocity fluctuations (Lee *et al.* 1997; Larsson & Lele 2009). The computational domain is $4\pi \times (2\pi)^2$ in the streamwise and transverse directions. Depending on the target flow state, 128^2–1024^2 grid points are used in the transverse plane and 512–4096 grid points, together with a non-uniform mesh which is finest around the shock, are used in the streamwise direction. The results presented in this paper are converged under grid refinement. This has been tested in several shorter simulations with single plane waves and turbulent fields, in which the mesh around the shock was kept uniform and refined up to four times the resolution used in the final calculations.

In order to provide realistic turbulence upstream of the shock wave, auxiliary forced IT simulations, with a background velocity matching the shock speed, are performed. The linear forcing method for compressible turbulence (Petersen & Livescu 2010) is used with the most energetic wavenumber, $k_0 = 4$, the ratio of dilatational to solenoidal kinetic energies, $\chi = 0.0005 \sim 0.12$ (quasi vortical turbulence), and $\eta/\Delta = 1.7 \sim 2.8$,

where Δ is the grid spacing. A discussion on the turbulence spectra resulting from this forcing method is provided in Petersen & Livescu (2010). The IT grid spacing is the same as the grid spacing in the transverse directions in the STI simulations. Here η/Δ of the present IT database has been chosen such that post-shock turbulence is also well resolved. The minimum value of η/Δ at the inflow of the STI domain is 1.7, becoming ~ 2 at the shock after the spatial decay. Larsson & Lele (2009) derived the formulation for the decrease of η across the shock wave. The largest decrease of η in this study is $\sim 40\%$ for $M_s = 2.2$, thus the smallest η/Δ is still larger than 0.8 behind the shock wave. For this value, the error of the compact scheme used here is small at the Nyquist scale relative to a spectral method with $\eta k_{max} = 1.5$ (Petersen & Livescu 2010). Plane data are recorded at a fixed plane perpendicular to the streamwise direction and the data are fed through the inlet of the STI domain. Here, the inlet turbulence is advected with the supersonic mean velocity and encounters a stationary shock wave. In previous studies, temporally decaying IT data was transformed into spatially decaying turbulence using Taylor's hypothesis. For compressible turbulence, this hypothesis has limitations at high M_t due to the ambiguity with acoustic wave propagation (Lee, Lele & Moin 1992). The present approach may become a good alternative for high-M_t flows or flows with a significant acoustic component. The turbulence statistics are collected after one flow-through time to remove the initial transients and the averages ($\langle \cdot \rangle$) are taken over time and transverse directions. At least three flow-through times are used to collect instantaneous data and the results are converged. The mean location of the shock is at streamwise position $x = 0$ and the turbulence quantities are non-dimensionalized by their values immediately upstream of the shock.

Figure 1 shows the parameter space considered in the present study. The M_s values are 1.1, 1.2, 1.4, 1.8 and 2.2. Here Re_λ immediately upstream of the shock varies between 10 and 45. Here M_{t2-LIA} is the post-shock turbulent Mach number computed using LIA for given upstream M_t and M_s. Here M_{t2-LIA} becomes the highest possible turbulent Mach number near the shock wave, assuming that viscous and nonlinear effects reduce the amplification. The comparison of M_{t2-LIA} with the downstream mean streamwise Mach number (M_{t2-LIA}/M_{s2}) may provide an indication for the linear interaction regime, as it represents an upper bound for the ratio between velocity fluctuations and mean velocity. Below or close to the lines of $M_{t2-LIA} = 0.1M_{s2}$, nonlinear effects may be small during the interaction and near the shock wave. The $M_t = 0.6(M_s - 1)$ curve divides the interaction regimes where the shock remains simply connected (wrinkled shock) and where it does not (broken shock) (Larsson *et al.* 2013). In this study, the parameter range covers the interaction regimes from linear inviscid, close to the LIA limit, to regimes dominated by nonlinear and/or viscous effects.

In the previous studies using LIA, only second-moment statistics have been examined. In order to compute the full post-shock flow fields, which are necessary to examine most of the higher-order quantities, one needs full flow fields in front of the shock as well. These fields are taken from separate forced IT DNS. The velocity fields are Fourier transformed and the solenoidal components are extracted using the Helmholtz decomposition (Livescu, Jaberi & Madnia 2002). Then, the complex LIA amplitude, A_v, is computed (the detailed LIA procedure can be found in Mahesh *et al.* 1997) and, after applying the LIA coefficients, a complete inverse Fourier transform is performed to recover the full velocity fields. Note that in previous studies the inverse Fourier transform was considerably simplified since the statistics required $|A_v|^2$ information only, which was extracted from the IT energy spectrum, $E(k)$, as $|A_v|^2 = E(k)/(4\pi k^2)$.
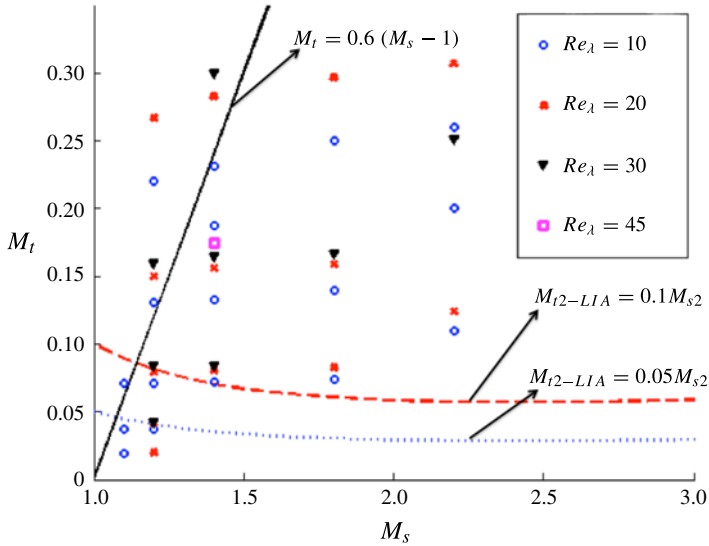
FIGURE 1. Parameter range for the simulations in the (M_t, M_s) domain. The regimes of the interaction can be asserted with the black line (above – broken shock, below – wrinkled shock) and the red-dashed or blue-dotted curves (below – linear effects dominate).
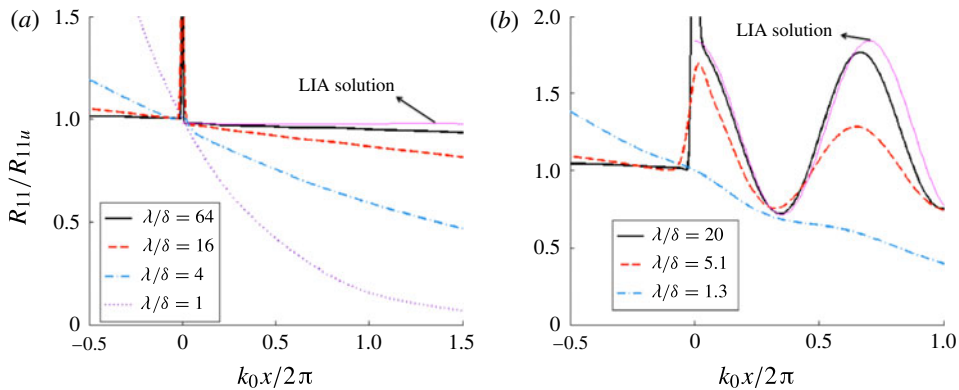
FIGURE 2. R_{11} variation through the shock for a single vortical plane wave from DNS and LIA at $M_s = 1.2$. (a) $\psi = 45°$ and (b) $\psi = 65°$. The top solid line represents the LIA solution.

3. Results

When there is a large separation in scale between the shock width and the incoming small-amplitude disturbances, viscous and nonlinear effects become negligible during the interaction process. In this case, the DNS results should be close to the LIA prediction. The interaction of a single vortical plane wave with a shock wave is considered in figure 2, following the set-up of Mahesh *et al.* (1997). The variation of the streamwise Reynolds stress ($R_{11} = \langle u'u' \rangle$) across the shock is compared between DNS and LIA. The LIA solution depends only on M_s and the angle between the
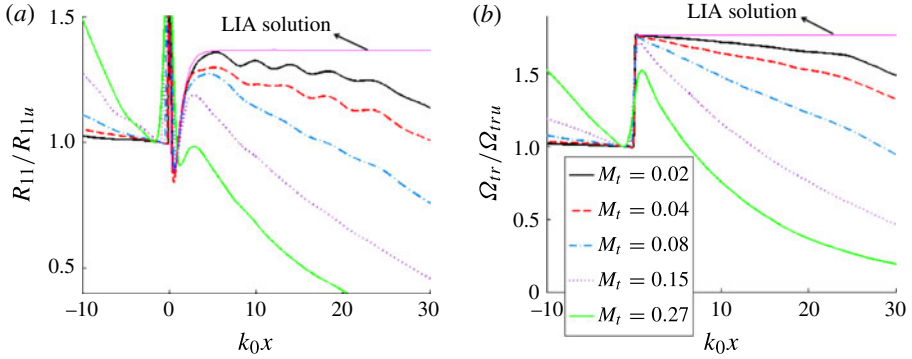
FIGURE 3. Convergence of (*a*) R_{11} and (*b*) Ω_{tr}, through a $M_s = 1.2$ shock to the LIA solution (top solid lines) as the nonlinear and viscous effects become small for the interaction. Here, $\delta/\eta = 2.3$, 1.3, 0.69, 0.34 and 0.17, as M_t decreases from 0.27 to 0.02. Here Re_λ is fixed at 20.

wavevector and streamwise direction, ψ, and is independent of the wavelength λ. When the ratio of λ to the laminar shock thickness δ is small, the DNS results are very different from the LIA solution, with the case $\lambda/\delta = 1$ showing no amplification at all. However, as λ/δ increases, the DNS results converge to the LIA prediction, even close to the critical angle (here, $\psi_{cr} \simeq 70°$). Here, ψ_{cr} is the angle at which the acoustic disturbance behind the shock changes its nature from a propagating to an attenuating wave and where the amplification increases sharply. This large amplification requires stronger constraints for the DNS to have small nonlinear effects. Thus, the results suggest that the scale separation can be a criterion for controlling the viscous effects on the interaction. Note that the figures do not show the full variation through the shock wave ($x = 0$ in figures 2 and 3*a*), in order to focus on the convergence to the LIA solution downstream of the shock. The rapid variations at $x = 0$ have been associated with the shock motion (Lee *et al.* 1993; Larsson *et al.* 2013).

The convergence to the LIA prediction is shown for full turbulent fields in figure 3. Here, the scale separation can be controlled by the ratio δ/η, which can be written as $\delta/\eta \simeq 7.69 M_t/(Re_\lambda^{0.5}(M_s - 1))$, and is varied by changing M_t. This expression was derived using fully developed homogeneous IT relations by Moin & Mahesh (1998) and proposed as a scale criterion for shock-capturing schemes. The DNS amplifications converge to the LIA solutions when δ/η becomes small. Note that the R_{11} convergence is slower than that of the transverse vorticity variance (Ω_{tr}). The peak location of Ω_{tr} is immediately behind the shock wave. However, the peak of R_{11} is located approximately one most energetic wavelength behind the shock and is affected by viscous effects after the shock interaction (Larsson *et al.* 2013) when Re_λ is small. These effects are minimized at fixed Re_λ as δ/η and M_t decrease, since the eddy turnover time and, consequently, the decay distance increase. Nevertheless, the viscous effects behind the shock lead to a slower R_{11} convergence to the LIA solution compared to Ω_{tr}.

The post-shock oscillations in figure 3(*a*) for the low-M_t cases are similar to those observed in Lee *et al.* (1997) and are not due to a lack of statistical convergence of the results, which has been carefully tested. Instead, our preliminary results seem to indicate that they may be associated with the critical angle and differences between
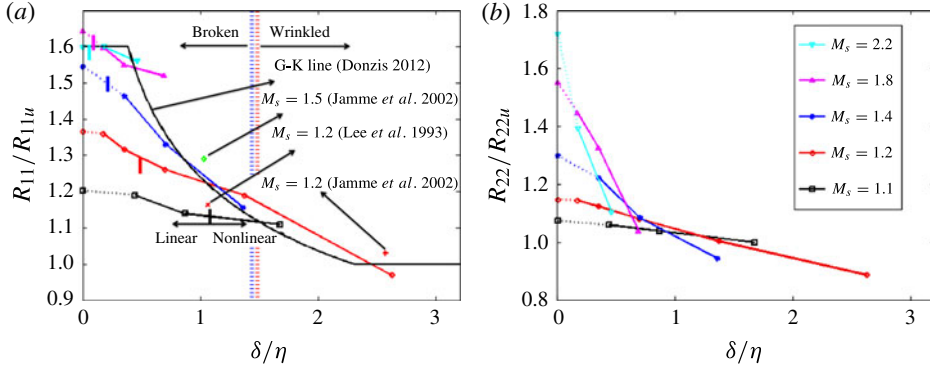
FIGURE 4. R_{11} and R_{22} amplifications from DNS as a function of δ/η for different M_s and $Re_\lambda \simeq 20$. Symbols along the vertical axis represent the LIA solutions with the shape and colour matched for the symbol-lines of the corresponding M_s. LIA solutions and corresponding DNS results are connected by dotted lines. The previous DNS results (Lee *et al.* 1993; Jamme *et al.* 2002) are shown with separate symbols. The black curve represents the amplification model from Donzis (2012). A short vertical bar separates linear and nonlinear regimes for each M_s by $M_{t2-LIA} = 0.1M_{s2}$.

the dilatational and solenoidal energies decay rates, which are exacerbated at low solenoidal energy (and M_t) levels. However, these oscillations seem to have little influence on the results immediately behind the shock, which are the main focus of this paper.

Figure 4 shows the convergence of the streamwise (R_{11}) and transverse ($R_{22} = \langle v'v' \rangle$) Reynolds stress amplifications from DNS to the LIA solutions, as M_t decreases, for all M_s values considered. The amplifications of the Reynolds stresses are computed as the ratio of the values at the location where R_{11} is maximum and immediately upstream of the shock, consistent with the LIA procedure. As most of the turbulence scales are much larger than δ, the viscous effects through the shock easily become negligible, even at $Re_\lambda \simeq 20$, and the results are not far from the LIA solution. Thus, it is stressed that even at low Re_λ, provided that M_t and, thus, δ/η are small enough, nonlinear and viscous effects across the shock become negligible and the amplification can be predicted by LIA. As expected, the convergence rate increases with Re_λ (figure 5b). Figure 5(a) shows the convergence of Ω_{tr}. The peak location of Ω_{tr} is immediately behind the shock wave and relatively large δ/η (large M_t) cases show very similar amplifications to the LIA.

The ratio δ/η, which combines the effects of M_t, M_s and Re_λ (see above), was proposed by Donzis (2012) as a universal parameter which characterizes the turbulence amplification (the G-K line in figure 4a). This is in contradiction to the LIA limit, which retains a separate M_s dependency as δ/η becomes small. The present simulations converge to the LIA solution as δ/η (and M_t) becomes small and exhibit the associated M_s dependence. There has been a long-standing open question about the significance of LIA theory (Lee *et al.* 1993, 1997; Mahesh *et al.* 1997; Jamme *et al.* 2002; Larsson & Lele 2009; Larsson *et al.* 2013). These results show that LIA is a reliable prediction tool when there is a scale separation between turbulence and the shock and M_t is small enough (additional comparisons with simulations are given below).

Previous studies have presented second-moment turbulence statistics using LIA and IT energy spectra. To investigate more detailed turbulence physics, which require
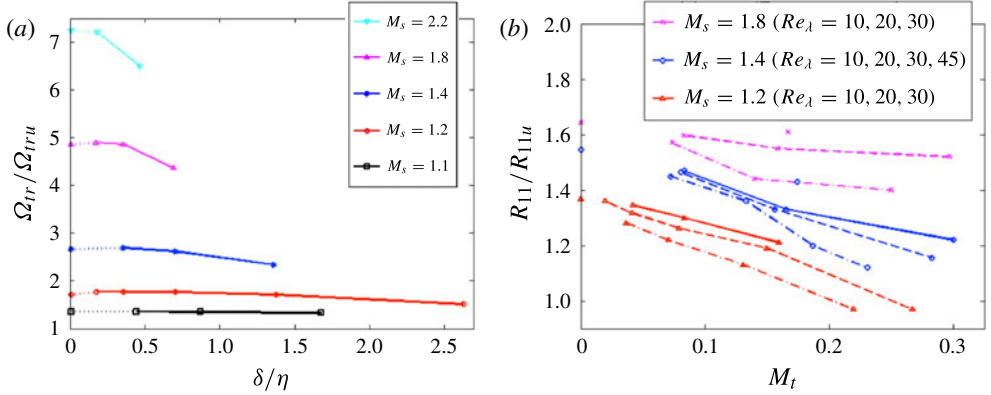
FIGURE 5. The amplifications of (*a*) Ω_{tr} for different M_s and $Re_\lambda \simeq 20$ and (*b*) R_{11} for different Re_λ and $M_s = 1.2$, 1.4 and 1.8, as a function of δ/η. Higher-Re_λ cases are located above the corresponding lower-Re_λ cases, showing faster convergence to the LIA prediction. Symbols along the vertical axis represent the LIA solution with the shape and colour matched for the symbol-lines of the corresponding M_s.

information beyond the incoming spectra of the primary variables, full flow fields are needed behind the shock wave. For this, we have extended the final form of the LIA formulae (see § 2 for more details) to use the full upstream flow fields. These fields are generated in separate IT simulations and, here, we present results corresponding to $Re_\lambda \simeq 100$, $M_t = 0.05$, $\chi \approx 0$ and $k_0 = 1$. Below, Shock-LIA and Shock-DNS refer to the post-shock fields computed using the LIA theory and DNS, respectively. Shock-LIA results at several M_s values are compared with the results from Shock-DNS and the original IT database.

In order to characterize the turbulent structures behind the shock wave, we have carried out an analysis of the invariant plane of the velocity gradient tensor (Perry & Chong 1987). The second, Q^*, and third, R^*, invariants of the anisotropic part of the velocity gradient tensor, $\boldsymbol{A}^* = \boldsymbol{A} - \theta/3\boldsymbol{I}$, where $\boldsymbol{A} = \nabla\boldsymbol{v}$ and $\theta = \nabla \cdot \boldsymbol{v}$, can reveal the distribution of these structures (Pirozzoli, Grasso & Gatski 2004; Wang *et al.* 2012). The (Q^*, R^*) joint probability density functions (PDFs) for the flow fields of IT, and upstream and downstream of the shock wave are shown in figure 6 at $M_s = 2.2$ and 6.0. The post-shock results are calculated at $k_0 x = 5$, which is after the peak of R_{11}, where the variations of the mean quantities are negligible compared to the contributions from the fluctuations and the turbulence decay is not yet significant. The axes are normalized by $Q_W = W_{ij}W_{ij}/2$, where $\boldsymbol{W}$ is the rotation tensor. The lateral lines denote the locus of zero discriminant of $\boldsymbol{A}^*$, $(27/4)R^{*2} + Q^{*3} = 0$. For IT and upstream of the shock wave, the joint PDF (figure 6*a,b*) exhibits the well-known tear-drop shape which has been previously observed in IT, boundary layers, mixing layers and channel flows (Pirozzoli *et al.* 2004; Wang *et al.* 2012), indicating that most data points have a local topology of stable-focus/stretching (second quadrant) or unstable-node/saddle/saddle (fourth quadrant). The shape is significantly modified across the shock (figure 6*c–f*), as the regions of stable-focus/compression (first quadrant) and stable-node/saddle/saddle (third quadrant) are enhanced. Shocked turbulence demonstrates a symmetrization of the (Q^*, R^*) joint PDF, similar to the high-expansion regions in forced compressible IT (Wang *et al.* 2012). As M_s is increased from 2.2 to 6.0 in figure 6(*c,d*), the normalized Q^* and R^* values decrease.
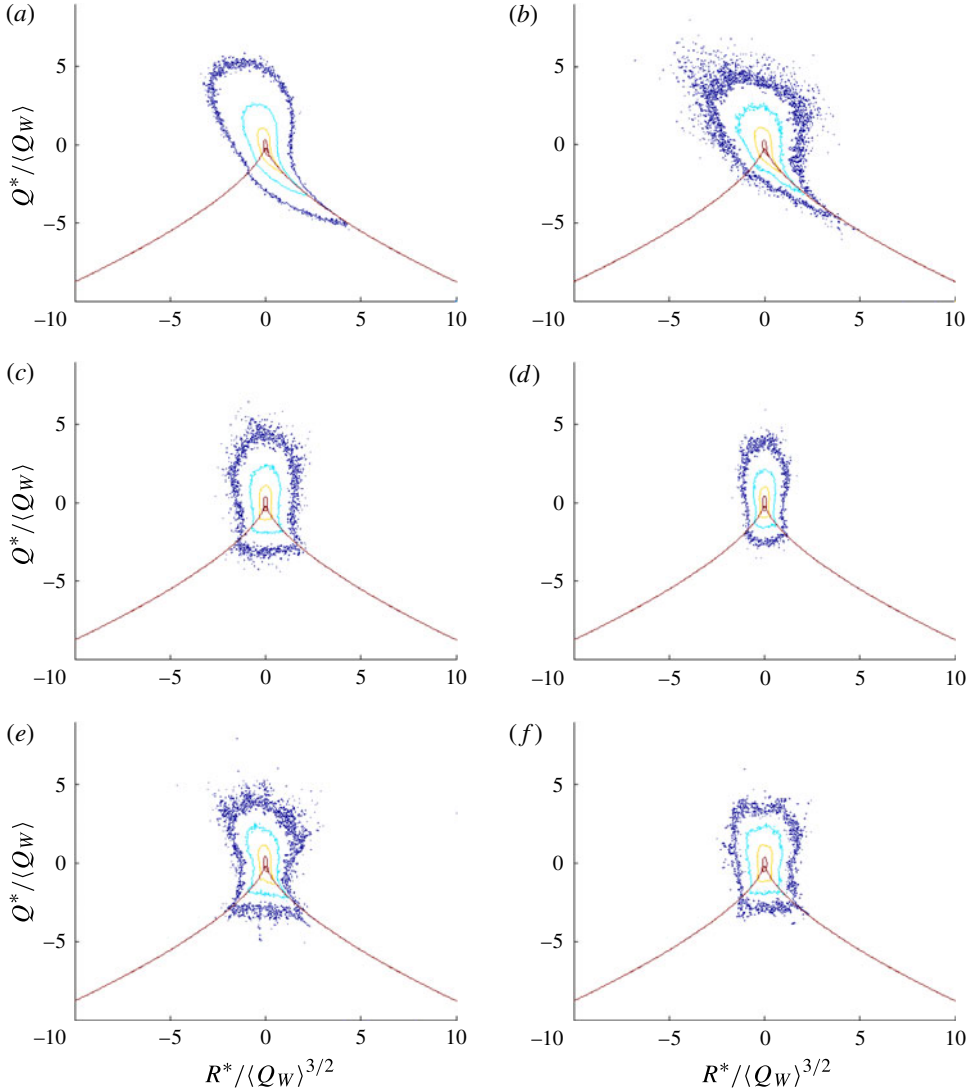
FIGURE 6. Iso-contour lines of $\log_{10}\text{PDF}(Q^*/\langle Q_W \rangle, R^*/\langle Q_W \rangle^{3/2})$ for (*a*) IT with $Re_\lambda \simeq 100$, (*b*) upstream of the shock wave with $Re_\lambda \simeq 20$, (*c*) and (*d*) Shock-LIA with $M_s = 2.2$ and 6.0 and $Re_\lambda \simeq 100$, (*e*) Shock-DNS with $M_s = 2.2$ and $Re_\lambda \simeq 20$, and (*f*) Shock-LIA with $M_s = 2.2$ and $Re_\lambda \simeq 20$. In each figure, four contour lines at 0, -1, -2, -3 are shown. The lateral lines denote the locus of zero discriminant.

These effects are further discussed below. Figure 6(*e*,*f*) show qualitatively similar symmetric joint PDF shapes for Shock-DNS and Shock-LIA at the same M_s and Re_λ, compared to the tear-drop distribution of IT and upstream of the shock wave.

The symmetrization of the (Q^*, R^*) joint PDF can be further explored with the unbiased measure of the deviatoric strain state, $\tilde{s}^* = (-3\sqrt{6}\tilde{\alpha}\tilde{\beta}\tilde{\gamma})/((\tilde{\alpha}^2 + \tilde{\beta}^2 + \tilde{\gamma}^2)^{3/2})$, where $\tilde{\alpha}$, $\tilde{\beta}$ and $\tilde{\gamma}$ are the eigenvalues of the deviatoric part of the strain rate tensor, $\boldsymbol{S}^*$ (Lund & Rogers 1994). In figure 7(*a*), the $\tilde{s}^*$ values for IT are clustered near $\tilde{s}^* = 1$, consistent with the morphology of the (Q^*, R^*) joint PDF. However, the post-shock
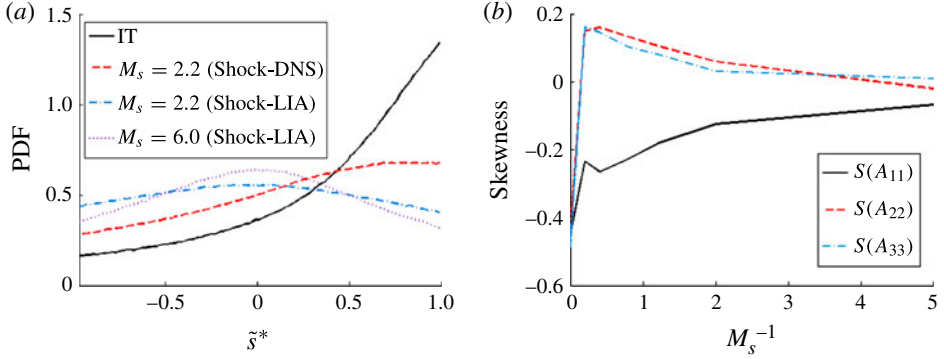
FIGURE 7. (*a*) PDF of $\tilde{s}^*$ for IT ($Re_\lambda \simeq 100$), two M_s cases using Shock-LIA with the IT database, and Shock-DNS with $Re_\lambda \simeq 20$. (*b*) Skewness of longitudinal velocity derivatives for IT and $M_s = 1.05$–6 using Shock-LIA ($Re_\lambda \simeq 100$).

fields exhibit a quasi-symmetric, relatively flat $\tilde{s}^*$ PDF. The symmetrization of the $\tilde{s}^*$ PDF (and, consequently, of the PDF of the β eigenvalue) implies a corresponding decrease in the vortex stretching term in the vorticity equation. The importance of the vortex stretching mechanism can also be inferred from the skewness of the longitudinal velocity derivatives. Figure 7(*b*) shows that the skewness for all three directions becomes small as M_s increases, suggesting an M_s-enhanced symmetrization of the PDFs of the corresponding longitudinal velocity derivatives. However, the variation of the kurtosis of the longitudinal velocity derivatives, K_t, (not shown here) becomes flat, with values around 4.0 at large M_s, so that non-Gaussian effects are still present.

Depending on the relation between the magnitude of the rotation, $W_{ij}W_{ij}$, and deviatoric strain, $S^*_{ij}S^*_{ij}$, the flow fields can be classified into regions of high rotational strain, *HRS*, where $W_{ij}W_{ij} > 2S^*_{ij}S^*_{ij}$, high irrotational strain, *HIS*, where $0.5S^*_{ij}S^*_{ij} > W_{ij}W_{ij}$, and highly correlated regions, *CS*, where $2S^*_{ij}S^*_{ij} \geqslant W_{ij}W_{ij} \geqslant 0.5S^*_{ij}S^*_{ij}$ (Pirozzoli *et al.* 2004). Figure 8 shows the joint PDFs of the normalized **W** and **S*** magnitudes. The post-shock fields show a significant increase, amplified with M_s, of P_{CS}. This increase is due to the preferential amplification of the transverse components of the two tensors, which can be inferred from the LIA solutions and explains the decrease in the normalized Q^* and R^* values shown above. Thus, the presence of the shock constrains the turbulence structures realizable, which, together with the reduction in the vortex stretching mechanism, reflects an M_s-mediated tendency towards an axisymmetric local state. The axisymmetric state has been explored for Reynolds stresses and vorticity variances in Lee *et al.* (1993, 1997) and Larsson & Lele (2009).

4. Summary and conclusions

A basic unit problem to study phenomena associated with the coexistence of shock waves and background turbulence is that of the interaction between IT and a normal shock wave. Although this has been extensively studied in the past, the significant computational requirements have limited the DNS studies to very low Reynolds numbers and/or large turbulent Mach numbers, as well as an overlap between the shock and turbulence scales. Experimental realizations of this problem are also very
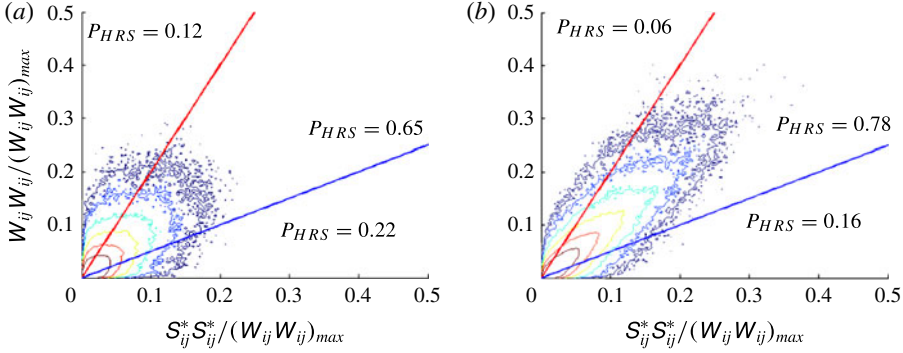
FIGURE 8. $\log_{10}$ PDF$(W_{ij}W_{ij}/(W_{ij}W_{ij})_{max},\ S^*_{ij}S^*_{ij}/(W_{ij}W_{ij})_{max})$ with six iso-contour lines, from -0.5 to 2.0. Shock-LIA results using the IT database with $Re_\lambda \simeq 100$ for (*a*) $M_s = 2.2$ and (*b*) $M_s = 6.0$. $(W_{ij}W_{ij})_{max}$ increases by factors of 5.42 and 19.7 for $M_s = 2.2$ and 6.0, respectively, compared to the original IT values. The fractions of the volumes occupied within the flow are shown for each region.

challenging, due to problems in controlling the shock wave and the small time and length scales involved in the measurements, especially close to the shock front. This has resulted in only limited agreement of the previous studies with the LIA predictions.

Here, we present an extensive set of DNS results on much larger meshes than previous studies and broadly covering the parameter range. For the first time, all Reynolds stress tensor and vorticity components from the DNS are shown to converge to the LIA solutions as viscous and nonlinear effects become small across the shock. The agreement obtained in the previous studies was limited to the turbulent kinetic energy only, while individual Reynolds stresses did not match the LIA solutions. The viscous effects become negligible for small values of δ/η due to the much shorter time scale of the interaction than that of the turbulence. Since $\delta/\eta \simeq 7.69 M_t/(Re_\lambda^{0.5}(M_s - 1))$, this ratio can be controlled using upstream M_t and Re_λ values. Using the DNS results, it is shown that δ/η, and thus the viscous effects across the shock, can be made arbitrarily small even at modest Re_λ, if M_t is sufficiently small, while small M_t values ensure negligible nonlinear effects as well. These results reconcile a long-standing open question about the role of LIA theory and establish LIA as a reliable prediction tool for problems with a large separation between the turbulence scales and the shock width, which are relevant to many practical applications. Furthermore, when this scale separation is large, the exact shock profile is no longer important in determining evolution across the shock, so that the LIA can be used to predict high-M_s interaction problems where fully resolved DNS is not feasible.

The classical LIA formulae have been extended to generate complete post-shock flow fields. The procedure is much cheaper than full STI simulations, thus allowing the study of post-shock turbulence at much larger M_s and Re_λ values than DNS of STI. The results show that the small-scale turbulent structures are modified considerably across the shock wave with: (i) a symmetrization of the third invariants of $\boldsymbol{A}^*$ and $\boldsymbol{S}^*$ and (M_s-mediated) of the PDF of the longitudinal velocity derivatives and (ii) an M_s-dependent increase in correlation between strain and rotation. Thus, the shock preferentially enhances the transverse components of the rotation and strain tensors,

which constraints the flow structures. This, together with a decrease in the vortex stretching mechanism, reflects a tendency towards an axisymmetric local state of the post-shock turbulence.

The results provided concern the region immediately after the shock, where the viscous effects are limited. As Re_λ increases, the size of this region also increases. Nevertheless, the spatial development of the shocked turbulence (e.g. a return to the isotropic state) can also be studied with separate spatial simulations using the Shock-LIA database, which is still an order of magnitude cheaper than DNS of the full STI problem.

Acknowledgements

References

AGUI, J. H., BRIASSULIS, G. & ANDREOPOULOS, Y. 2005 Studies of interactions of a propagating shock wave with decaying grid turbulence: velocity and vorticity fields. *J. Fluid Mech.* **524**, 143–195.

ANDREOPOULOS, Y., AGUI, J. H. & BRIASSULIS, G. 2000 Shock wave–turbulence interactions. *Annu. Rev. Fluid Mech.* **32**, 309–345.

BARRE, S., ALEM, D. & BONNET, J. P. 1996 Experimental study of a normal shock/homogeneous turbulence interaction. *AIAA J.* **34**, 968–974.

DONZIS, D. A. 2012 Amplification factors in shock–turbulence interactions: effect of shock thickness. *Phys. Fluids* **24**, 011705.

FREUND, J. B. 1997 Proposed inflow/outflow boundary condition for direct computation of aerodynamic sound. *AIAA J.* **35**, 740.

JAMME, S., CAZALBOU, J. B., TORRES, F. & CHASSAING, P. 2002 Direct numerical simulation of the interaction between a shock wave and various types of isotropic turbulence. *Flow Turbul. Combust.* **68**, 277.

LARSSON, J., BERMEJO-MORENO, I. & LELE, S. K. 2013 Reynolds- and Mach-number effects in canonical shock–turbulence interaction. *J. Fluid Mech.* **717**, 293.

LARSSON, J. & LELE, S. K. 2009 Direct numerical simulation of canonical shock/turbulence interaction. *Phys. Fluids* **21**, 126101.

LEE, S., LELE, S. K. & MOIN, P. 1992 Simulation of spatially evolving turbulence and the applicability of Taylor's hypothesis in compressible flow. *Phys. Fluids* **4**, 1521.

LEE, S., LELE, S. K. & MOIN, P. 1993 Direct numerical simulation of isotropic turbulence interacting with a weak shock wave. *J. Fluid Mech.* **251**, 533.

LEE, S., LELE, S. K. & MOIN, P. 1997 Interaction of isotropic turbulence with shock waves: effect of shock strength. *J. Fluid Mech.* **340**, 225.

LELE, S. K. 1992 Compact finite difference schemes with spectral-like resolution. *J. Comput. Phys.* **103**, 16.

LIVESCU, D., JABERI, F. A. & MADNIA, C. K. 2002 The effects of heat release on the energy exchange in reacting turbulent shear flow. *J. Fluid Mech.* **450**, 35.

LIVESCU, D., MOHD-YUSOF, J., PETERSEN, M. R. & GROVE, J. W. 2009 CFDNS: a computer code for direct numerical simulation of turbulent flows. LA-CC-09-100, LANL.

LUND, T. S. & ROGERS, M. M. 1994 An improved measure of strain state probability in turbulent flows. *Phys. Fluids* **6**, 1838.

MAHESH, K., LELE, S. K. & MOIN, P. 1997 The influence of entropy fluctuations on the interaction of turbulence with a shock wave. *J. Fluid Mech.* **334**, 353.

MOIN, P. & MAHESH, K. 1998 Direct numerical simulation: a tool in turbulence research. *Annu. Rev. Fluid Mech.* **30**, 539–578.

MOORE, F. K. 1954 Unsteady oblique interaction of a shock wave with a plane disturbance. NACA TR-1165.

PERRY, A. E. & CHONG, M. S. 1987 A description of eddying motions and flow patterns using critical-point concepts. *Annu. Rev. Fluid Mech.* **19**, 125.

PETERSEN, M. R. & LIVESCU, D. 2010 Forcing for statistically stationary compressible isotropic turbulence. *Phys. Fluids* **22**, 116101.

PIROZZOLI, S., GRASSO, F. & GATSKI, T. B. 2004 Direct numerical simulations of isotropic compressible turbulence: influence of compressibility on dynamics and structures. *Phys. Fluids* **16**, 4386.

RIBNER, H. S. 1954 Convection of a pattern of vorticity through a shock wave. NACA TR-1164.

WANG, J., SHI, Y., WANG, L., XIAO, Z., HE, X. T. & CHEN, S. 2012 Effect of compressibility on the small-scale structures in isotropic turbulence. *J. Fluid Mech.* **713**, 588.